

This is the accepted manuscript made available via CHORUS. The article has been published as:

Local structural distortions, orbital ordering, and  
ferromagnetism in underdoped  $\text{La}_{1-x}\text{Sr}_x\text{MnO}_3$

J.-S. Zhou and J. B. Goodenough

Phys. Rev. B **91**, 064414 — Published 17 February 2015

DOI: [10.1103/PhysRevB.91.064414](https://doi.org/10.1103/PhysRevB.91.064414)

# Local structural distortions, orbital ordering, and ferromagnetism in underdoped $\text{La}_{1-x}\text{Sr}_x\text{MnO}_3$

J.-S. Zhou\* and J.B. Goodenough

Materials Science and Engineering Program, Mechanical Engineering, University of Texas at Austin,  
Austin, TX 78712

In order to elucidate the origin of the ferromagnetism found in underdoped  $\text{La}_{1-x}\text{Sr}_x\text{MnO}_3$ , we have grown a series of single crystals with a fine step of doping and characterized them by a structural study, measurements of magnetization, resistivity, thermoelectric power, and thermal conductivity. The paramagnetic phase of the underdoped  $\text{La}_{1-x}\text{Sr}_x\text{MnO}_3$  is a small-polaron conductor. However, the Weiss constant extracted from the paramagnetic susceptibility shows a ferromagnetic coupling and tracks the Curie temperature. Given that the double exchange interaction cannot be delivered by the hopping motion of small polarons, we have made a systematic analysis of the structural changes with  $x$  and studied whether the superexchange interaction can actually account for the ferromagnetic coupling found in the paramagnetic phase. Intrinsic local site distortions in  $\text{LaMnO}_3$  change as  $x$  increases in  $\text{La}_{1-x}\text{Sr}_x\text{MnO}_3$ . The influence of the local structural distortion and the cooperative orbital ordering on the  $\text{Mn}^{3+}$  sites has been demonstrated by a comparison between the measured change of lattice parameters versus hole doping and a simulation with the software SPuDs in which rigid octahedra are assumed. Changes with  $x$  of the splitting of the bond lengths of  $\text{MnO}_6$  octahedra induces an orbital mixing of  $3x^2 - r^2/y^2 - z^2$  ( or  $3y^2 - r^2/z^2 - x^2$  ), which progressively converts 2D ferromagnetism in the parent perovskite  $\text{LaMnO}_3$  into 3D ferromagnetism. The correlation between the particular lattice distortions and the cooperative orbital ordering and orbital mixing can in turn be used to test the superexchange model by measuring the change of transition temperatures under uniaxial stress. Nearly identical uniaxial stress effects found in crystals of the mixed valent  $\text{La}_{0.875}\text{Sr}_{0.125}\text{MnO}_3$  and single-valent  $\text{LaMn}_{0.5}\text{Ga}_{0.5}\text{O}_3$  confirm unambiguously that superexchange interactions play the dominant role in the ferromagnetic coupling of underdoped  $\text{La}_{1-x}\text{Sr}_x\text{MnO}_3$ .

## Introduction

The concept of a double exchange (DE) ferromagnetic interaction introduced by Zener <sup>1</sup> has been believed to be applicable to the ferromagnetism in the mixed-valent manganites  $\text{La}_{1-x}\text{A}_x\text{MnO}_3$  (A=Ca, Sr, Ba) that exhibit a colossal magnetoresistance in the vicinity of the Curie temperature. The hole doping changes transport properties and induces an antiferromagnetism to ferromagnetism transition. In this paper, we question whether the DE interaction indeed plays a dominant role in the magnetic interaction of the underdoped manganites  $\text{La}_{1-x}\text{Sr}_x\text{MnO}_3$ .

The original Hamiltonian for the DE interaction in manganites consists of two terms, the hopping term and the Hund coupling term. An  $e_g$  electron on site  $i$  while coupled strongly to the spin of the core  $t_2^3$  electrons through the Hund coupling can hop to an empty  $e_g$  orbital on site  $j$  due to quantum spin fluctuations regardless of the core spin orientation between the two sites. An electron travelling through a spin disordered matrix would gain a kinetic energy if core spins on the neighboring sites are parallel, which effectively delivers a ferromagnetic coupling. The original treatment by Anderson and Hasegawa <sup>2</sup> of the DE Hamiltonian gave no magnetic coupling in the paramagnetic phase, *i.e.* the paramagnetic susceptibility fitting to a Curie law. Anderson realized the mistake later in a book chapter <sup>3</sup> and referred to the treatment by de Gennes. <sup>4</sup> However, as seen from the paramagnetic  $\chi^{-1}(T)$ , the ferromagnetism derived by de Gennes comes as the system with antiferromagnetic coupling is cooled down. Millis <sup>5</sup> has expanded the double exchange interaction in doped manganites by including the Coulomb interaction between  $e_g$  electrons and the electron-phonon interactions. However, whether ferromagnetic coupling can be resolved in the phase with small polaron conduction is questionable. As shown in this paper, the Weiss constant obtained from fitting the paramagnetic susceptibility of underdoped  $\text{La}_{1-x}\text{Sr}_x\text{MnO}_3$  to a Curie-Weiss law tracks the magnetic-ordering temperature as in a normal material where the Weiss molecular-field parameter  $\theta_w$  is the same as the spin ordering temperature  $T_c$ .

In addition to the DE interaction through a real  $e_g$ -electron transfer, the virtual charge transfers between localized electrons on manganese ions result in a superexchange interaction that either reinforces or competes with any DE interaction. In  $\text{La}_{1-x}\text{Sr}_x\text{MnO}_3$ , the localized  $t_{2g}^3$  electrons give an antiferromagnetic superexchange coupling by a virtual charge transfer between half-filled

orbitals on two neighbor Mn in both  $\text{LaMnO}_3$  and  $\text{SrMnO}_3$ ; any ferromagnetic coupling must come from the  $\sigma$ -bonding  $e_g^1$  electrons of the high-spin  $\text{Mn}^{3+}$   $\text{La}_{1-x}\text{Sr}_x\text{MnO}_3$ . If real charge transfer of the  $e_g^1$  electron to a neighboring  $\text{Mn}^{4+}$  ion is too slow, as in the case for small-polaron hopping, the DE mechanism is inoperative; but a virtual transfer of  $e_g^1$  electron to an empty  $e_g$  orbital on a neighboring Mn provides a ferromagnetic superexchange interaction. In  $\text{LaMnO}_3$  with a  $T_N \approx 145$  K, <sup>6</sup> ordering of the  $e_g$  electrons in the (001) planes provides a 2D ferromagnetic superexchange, but along the  $c$ -axis the antiferromagnetic interactions between the  $\pi$ -bonding  $t_{2g}^3$  states are dominant. In  $\text{SrMnO}_3$  where there are no  $e_g$  electrons, type-G antiferromagnetic order (all near neighbor spins antiparalleled) with  $T_N \approx 233$  K <sup>7</sup> provides clear evidence that the superexchange interactions are strong enough to account for the magnetic-order transition in underdoped  $\text{La}_{1-x}\text{Sr}_x\text{MnO}_3$ . However, to achieve a 3D ferromagnetism by superexchange interactions, the  $e_g$  orbital order on the  $\text{Mn}^{3+}$  must provide some  $e_g$ -electron orientation along the  $c$  axis as well as in  $a$ - $b$  planes. In addition to creating a mixture of  $\text{Mn}^{3+}/\text{Mn}^{4+}$  if the  $e_g$  electrons remain localized, the Sr doing in  $\text{La}_{1-x}\text{A}_x\text{MnO}_3$  also changes the local site distortions similar to their change in the single-valent system  $\text{LaMn}_{1-x}\text{Ga}_x\text{O}_3$ . The local structural change in  $\text{LaMn}_{1-x}\text{Ga}_x\text{O}_3$  causes an evolution from 2D ferromagnetic coupling to 3D ferromagnetic coupling. There is no doubt that the magnetic coupling involved in the evolution from 2D to 3D ferromagnetism in  $\text{LaMn}_{1-x}\text{Ga}_x\text{O}_3$  is due to the superexchange interaction in this single-valent system. The central question we ask in this paper is *how to extract the structural-change that induces an evolution of the superexchange interaction in doped mixed-valent manganites and whether it is actually responsible for the transition from the type-A antiferromagnetic spin order to a ferromagnetic spin ordering.*

We have designed and performed the following experiments in order to address these questions: (1) Systematic measurements of the paramagnetic susceptibility and the study of crystal structure in the underdoped  $\text{La}_{1-x}\text{Sr}_x\text{MnO}_3$  crystals with fine steps of  $x$ . (2) The  $x=0.125$  sample undergoes a cooperative orbital-order transition, a ferromagnetic transition, and a charge ordering transition as temperature decreases; we have made a close comparison between its magnetic and transport properties as well as its thermal conductivity in order to clarify whether the magnetic coupling is correlated to a real charge transfer. (3) The evolution of the superexchange interaction in doped manganites, if it plays a dominant role, relies on a change in the cooperative orbital-order

distortion and the orbital mixing. Since these changes correspond to particular lattice distortions, measurements of physical properties under uniaxial stress would provide a critical test of the model. The uniaxial stress effects on  $T_c$  in the  $x=0.125$  crystal have been directly compared with that in the single-valent crystal  $\text{LaMn}_{0.5}\text{Ga}_{0.5}\text{O}_3$ .

Since intrinsic octahedral-site distortions in the orthorhombic  $Pbnm$  perovskite structure bias the orbital order and associated orbital mixing, a structural study must be reviewed first to build the foundation for understanding the evolution of the magnetic order in the underdoped  $\text{La}_{1-x}\text{Sr}_x\text{MnO}_3$  system. In this system, the  $Pbnm$  structure of the underdoped region converts to the rhombohedral  $R-3c$  structure only at a higher level of  $x$ . In addition to the well-known cooperative octahedral-site rotations in the  $Pbnm$  structure, intrinsic octahedral-site distortions occur and change their character with increasing rotation angle as the mean size of the A-site cation decreases. We elaborate two components of the intrinsic site distortions that vary with the site rotation and analyze how uniaxial stress influence these distortions and their bias effects on the cooperative orbital ordering, spin ordering, and charge ordering.

## Experimental detail

Crystals of  $\text{La}_{1-x}\text{Sr}_x\text{MnO}_3$  ( $0 \leq x \leq 0.18$ ) were grown by the floating-zone method with an image furnace (NEC M-35HD). The polycrystalline rods used for the feed and seed rods were prepared from a stoichiometric mixture of  $\text{La}_2\text{O}_3$ ,  $\text{SrCO}_3$ , and  $\text{Mn}_2\text{O}_3$  that had been synthesized at temperatures  $950^\circ\text{C}$  -  $1150^\circ\text{C}$  with inter-anneal grindings. The powder samples were pressed into rods that were sintered at  $1250^\circ\text{C}$  for 24 h. The  $\text{La}_{1-x}\text{Sr}_x\text{MnO}_3$  crystals with  $0 \leq x \leq 0.1$  were grown in Ar; those with  $x > 0.1$  were grown in flowing air. The same procedure was used by Urushibara *et al.*<sup>8</sup> they have checked the samples' stoichiometry by the inductance charge plasma (ICP) method. Powder X-ray diffraction (XRD) was performed on pulverized crystals in a Philips X'pert diffractometer with scan step  $0.02^\circ/5\text{s}$ . Lattice parameters have been obtained by refining XRD data with the Rietveld method (FULLPROF program). The magnetic and transport properties were measured with a Physical Property Measurement System (PPMS) and a Superconducting Quantum Interfering Device (SQUID). Measurements of thermal conductivity and thermoelectric power were performed with home-made setups; the steady-state method was used in the measurement for thermal conductivity.

The device used for the magnetization under uniaxial stress is similar to that reported in ref. 9. The cell body is made of BeCu with two ZrO<sub>2</sub> rods ground with high precision and having a fine surface finish. The rod's end surface contacting a crystal was coated with a layer of Kapton tape. Two Kapton-tape rings outside the cell body were used to guide the cell straight inside the bore of a SQUID magnetometer. The loading force was measured by the shifting of the superconductive T<sub>c</sub> of a small piece of Pb placed in a miniature piston cylinder inside the cell. The spring pushing rod in the cell was used to absorb any stress that is not parallel to the axis of the cylindrical cell body.

## Results and Discussion

1. The local octahedral-site distortions in the orthorhombic perovskite structure.
  - (1) The intrinsic angular octahedral-site distortion and its bias on the cooperative orbital ordering.

The AMO<sub>3</sub> perovskite structure consists of a 3D framework of corner-shared MO<sub>6</sub> octahedra and a body-centered A cation. The cubic structure occurs where the geometric tolerance factor is  $t = (A-O)/[\sqrt{2}(M-O)] = 1$ , where A-O and M-O are the equilibrium bond lengths. The structure responds to a  $t < 1$  by cooperative octahedral-site rotations.

The major octahedral-site rotation axis in the orthorhombic perovskite with the *Pbnm* setting is the *b* axis. This cooperative rotation makes the lattice parameters  $a < b$  if the octahedra are rigid. However, it has been demonstrated in single-valent systems that the *b* axis starts to reduce and eventually crosses the *a* axis where the O<sub>21</sub>-M-O<sub>22</sub> bond angle  $\alpha$  in the *a-b* plane, see the definition of the bond angle in the inset of Fig.1, becomes less than 90°. <sup>10</sup> It is interesting to note that the *b*-axis reduction sets in where the bond length splitting distortion reaches a maximum as the *t* factor increases. <sup>10,11</sup> Although the influence of the angular distortion on lattice parameters is obvious, *i.e.* *b* crossing *a*,  $\alpha$  typically deviates from 90° by just 1°. <sup>12</sup> Such a small deviation is within error bars for most diffraction studies and can only be discerned unambiguously by a systematic change of  $\alpha$  versus *t* in some well-studied systems <sup>13</sup> like RCrO<sub>3</sub> and RFeO<sub>3</sub> (R = Y or rare-earth). The anomaly in the *b* versus (IR) of the A-site cation and *b* crossing *a* serve as good indicators for monitoring the bond angle  $\alpha$ . Up to this point, we have demonstrated the intrinsic site distortion without involving the issue of how the distortion biases orbital ordering of the Mn<sup>3+</sup> e<sub>g</sub> electrons.

In the mixed valent system  $\text{La}_{1-x}\text{Sr}_x\text{MnO}_3$ , the bond length mismatch due to a  $t < 1$  in the parent compound  $\text{LaMnO}_3$  is continuously improved by the Sr substitution, which creates smaller  $\text{Mn}^{4+}$  cations at the M-site.<sup>8,14, 15</sup> Although there is a large body of structural studies in the literature,<sup>15,16,17, 18</sup> none of these works have clarified the evolution of lattice parameters in the context of changing the  $\text{O}_{21}\text{-Mn-O}_{22}$  bond angle and the relationship between the angular site distortion and the cooperative orbital ordering.

In order to understand the evolution of lattice parameters as a function of  $x$ , we have first made a simulation of lattice parameters for the series  $\text{La}_{1-x}\text{Sr}_x\text{MnO}_3$  in Fig.1(a) by using the software SPuDS.<sup>19</sup> Rigid octahedra are presumed in the algorithm of the SPuDS. In contrast to the overall trend of lattice parameters versus IR (and therefore the  $t$  factor) predicted by SPuDS for the single-valent systems  $\text{RMO}_3$  where  $a$ ,  $b$ , and  $c$  increase with IR, the lattice parameters of the mixed-valent  $\text{La}_{1-x}\text{Sr}_x\text{MnO}_3$  system calculated from SPuDS shrink monotonically as Sr doping increases, which is consistent with a continuously reduced Mn-O bond length as the hole doping increases in the system. It is also important to note that the simulation which ignores the bias of a site distortion, takes into account a cooperative orbital-order distortion in this manganite system so that a  $c/\sqrt{2} < a$  is obtained ( $c/\sqrt{2} > a$  holds for the JT-inactive systems like  $\text{RCrO}_3$  and  $\text{RFeO}_3$ ).<sup>13</sup> It is clear from the simulation that the transition from the orthorhombic phase to a cubic perovskite  $a^0a^0a^0$  phase at a critical Sr doping can be made by continuously reducing the tilting angle in the  $a^+a^+c^-$  tilting system of the orthorhombic phase. On the other hand, a systematic experimental study of tilting systems for the perovskite structure<sup>20</sup> shows that the connection between the orthorhombic phase  $a^+a^+c^-$  and a cubic phase  $a^0a^0a^0$  is made through a second-order transition to a tetragonal phase with the tilting system  $a^0a^0c^+$ . The stabilization of the tetragonal phase is clearly missed in the simulation with SPuDs.

Now we turn to the measured results plotted in Fig.1(b) for  $\text{La}_{1-x}\text{Sr}_x\text{MnO}_3$ . In comparison with the simulation results from the SPuDS, a dramatic difference is that the orthorhombic  $Pbnm$  phase does not transform into a cubic phase by increasing the hole doping. Instead, the system undergoes at least one phase transition; it is the rhombohedral  $R-3c$  phase in this case. In the diagram of tilting systems for the perovskite structure, the transition from an orthorhombic  $Pbnm$  phase to a rhombohedral  $R-3c$  phase cannot be realized by reducing tilting components continuously; therefore, the transition must be first order, which is confirmed by this work. The

first-order transition to the  $R-3c$  phase is commonly seen for a single valent  $A^{3+}B^{3+}O_3$  system and mixed-valent orthorhombic perovskites as the bonding mismatch is improved by increasing the  $t$  factor or under hydrostatic pressure.<sup>21-27</sup> A first-order transition to a different orthorhombic  $Imma$  phase has been seen for the orthorhombic  $A^{2+}B^{4+}O_3$  perovskites as the  $t$  factor increases.

28-32

The reason that the orthorhombic phase cannot transform into a cubic phase by reducing tilting components is rooted in a general argument: it is not possible to link together a 3D network of perfect octahedra in a system with fixed rotation axes.<sup>33</sup> Therefore, the change of octahedral-site tilting in a real system is always accompanied by different local site distortions. The deviation of the O-M-O bond angle from  $90^\circ$  is the dominating site distortion for the  $Pbnm$  perovskites at larger  $t$ . A pseudo-tetragonal phase  $a \approx b$  ( $\approx c/\sqrt{2}$  in the cases of a pseudo cubic phase) can result where the  $\alpha$  angle deviates from  $90^\circ$  by as small as  $\Delta\alpha = 90 - \alpha = 1.5^\circ$ . The pseudo-cubic phase, however, should be distinguished from the cubic phase at  $x_c$  in the simulated results by SPuDS in Fig.1(a). It is always found that  $b$  crossing  $a$  is followed by a continuous increase of  $a-b$  as the  $t$  factor further increases, which also signals that  $\Delta\alpha$  increases continuously. The structure is frustrated by an enhanced  $\alpha < 90^\circ$  site distortion as the octahedral-site rotations are reduced. Relieving the structural frustration must be the major driving force for the phase transition to either the  $R-3c$  or  $Imma$  phase. As an indicator for the  $\alpha < 90^\circ$  site distortion, the observations of  $b$  crossing  $a$  and a following increase of  $a-b$  in the  $Pbnm$  phase becomes the precursor for the phase transition.

The cooperative orbital-order distortion in the parent compound  $LaMnO_3$  makes the lattice parameters  $a > c/\sqrt{2}$ , it is  $a < c/\sqrt{2}$  in the orbitally non-degenerate or the orbitally disordered systems. The criteria<sup>34</sup> for identifying a cooperative orbital-order distortion had been put forward long before the neutron diffraction and the Retveld refinement were widely applied. The cooperative orbital-order distortion enhances the orthorhombic strain factor  $s \equiv 2(b-a)/(b+a)$ , which has been pointed out previously<sup>35</sup> and can also be easily recognized by comparing lattice parameters from the prediction by the SPuDS simulation (even if the orbital-order distortion on  $Mn^{3+}$  is included) and the measurement results for the parent compound  $LaMnO_3$  in Fig.1. Enhancing the  $s$  factor alone does not clarify whether the angular distortion still takes place in the orbitally ordered phase. The hole doping reduces gradually the magnitude of a cooperative



orbital order distortion; a complete suppression of the cooperative orbital order distortion occurs near  $x \approx 0.12$  where  $c/\sqrt{2}$  exhibits a drastic jump and crosses  $b$  as the hole doping further increases. In the orbitally ordered phase for  $x < 0.11$ ,  $b$  and  $a$  show a linear dependence as a function of  $x$ . Extrapolating these two lines leads to  $b$  crossing  $a$  within the  $Pbnm$  phase, which indicates that the  $\Delta\alpha$  for the cooperative orbitally ordered phase is close to  $1.5^\circ$  at point A ( $x \approx 0.13$ ) in Fig.1(b). On the other hand, the orbital disordered phase also shows an angular site distortion;  $b \approx a$  occurs at point B ( $x \approx 0.075$ ) obtained by extrapolating the linear fitting of  $b$  versus  $x$  and  $a$  versus  $x$  in Fig.1(b). Generally speaking,  $\Delta\alpha$  increases as  $x$  increases for both the cooperative orbital order and the orbitally disordered phases, but  $\Delta\alpha$  reaches  $1.5^\circ$  at  $x \approx 0.075$  for the orbitally disordered phase whereas it is at  $x \approx 0.13$  for the phase with cooperative orbital ordering. A remarkable collapse of lattice parameter  $b$  near  $x \approx 0.09$  indicates an abrupt increase of  $\Delta\alpha$  for the orbitally disordered phase. It is clear that while the intrinsic angular site distortion still takes place in the phase with a cooperative orbital-order distortion, the  $e_g$  Jahn-Teller (JT) distortion, which would be primarily  $3x^2-r^2$  or  $3y^2-r^2$  on the neighboring two Mn sites in the  $a$ - $b$  plane of the orthorhombic perovskite, reduces significantly the magnitude  $\Delta\alpha$  of the site distortion. This observation in turn suggests that *a cooperative JT distortion of the  $e_g$  electrons prefers the octahedral site with the  $O_{21}$ -Mn- $O_{22}$  bond angle  $\alpha = 90^\circ$ .*

(2) The local site bond-length splitting distortion and the orbital mixing.

The intrinsic site distortion found in JT-inactive systems such as  $RFeO_3$  shows the bond length splitting into long, medium and short M-O bonds in the  $MO_6$  octahedra. As the rare earth IR reduces, the bond length splitting shows an evolution that is universal for all JT-inactive orthorhombic perovskites  $RMO_3$ .<sup>11</sup> The intrinsic site distortion biases orbital ordering and orbital mixing. The cooperative orbital order distortion in  $LaMnO_3$  orders the  $e_g$  electron into  $3x^2-r^2$  and  $3y^2-r^2$  at two neighboring  $Mn^{3+}$  in an  $ab$  plane. The orbital ordering would produce a corresponding site distortion with four short and two long Mn-O bonds in an octahedron. Kanamori<sup>36</sup> has recognized the structural bias effect on the orbital ordering based on long, medium and short Mn-O bonds found in  $LaMnO_3$ . The site distortion indicates that  $e_g$  electrons actually occupy a mixture of orbitals  $(3x^2-r^2) + (y^2-z^2)$  or  $(3y^2-r^2) + (z^2-x^2)$ . As the  $t$  factor reduces in  $RMnO_3$  perovskites, the orbital mixing changes by following the bias effect from the intrinsic site distortion for the  $Pbnm$  perovskite.<sup>37</sup> The Ga substitution in  $LaMn_{1-x}Ga_xO_3$  reduces

the bond length splitting,<sup>38</sup> but it also alters the orbital mixing in such a way that it induces a transition from 2D to 3D ferromagnetism<sup>39</sup> in this single valent insulator system. The local distortion in  $\text{LaMn}_{1-x}\text{Ga}_x\text{O}_3$  serves as a template to show the degree of the orbital mixing required for the 2D to 3D ferromagnetic transition. As shown in Fig.2, the local site distortion in  $\text{La}_{1-x}\text{Sr}_x\text{MnO}_3$ <sup>16</sup> matches stunningly well that in  $\text{LaMn}_{1-x}\text{Ga}_x\text{O}_3$ . The structural study suggests that ferromagnetism in the underdoped  $\text{La}_{1-x}\text{Sr}_x\text{MnO}_3$  could come from the same superexchange interaction as in  $\text{LaMn}_{1-x}\text{Ga}_x\text{O}_3$ . It should be noted that the bond length splitting in  $\text{La}_{1-x}\text{Sr}_x\text{MnO}_3$  vanishes at the phase boundary  $x \approx 0.165$ ; in the rhombohedral phase for  $x > 0.165$ , the structural symmetry allows only a single Mn-O bond length. The O/R phase boundary obtained from Fig.2 is consistent with that from Fig.1. **It should be noted that the O'/O\* transition at  $x \approx 0.11$  from Fig.1 does not correspond to an abrupt change in the bond length splitting.** As for the  $\text{LaMn}_{1-x}\text{Ga}_x\text{O}_3$ , the entire series crystallizes in the *Pbnm* structure, so that a complete collapse of the bond length splitting is not expected. However, the disorder of Ga/Mn on the B site makes it difficult to resolve the bond length splitting for  $x > 0.6$  by using a diffraction experiment.

The cooperative orbital ordering in  $\text{LaMnO}_3$  places  $e_g$  electrons primarily into the *ab* planes. The magnetic coupling along the *c* axis is from the superexchange interaction via the  $t^3\text{-O-}t^3$  interaction, which is antiferromagnetic. The orbital ordering leads to not only the cell distortion with a reduced *c* axis ( $c/\sqrt{2} < a$ ), but also the reduced Mn-O<sub>1</sub> bond length ( $\text{Mn-O}_1 < (\text{Mn-O}_2)_{\text{av}}$ ). As seen from the structural change, both Ga substitution and the hole doping increase the occupation of  $e_g$  electrons in the orbital along the *c* axis. An increased occupation of  $e_g$  electrons along the *c* axis builds a ferromagnetic coupling that eventually overcomes the antiferromagnetic coupling from  $t^3\text{-O-}t^3$  interaction along this direction. The relationship between the lattice distortion and magnetic coupling suggests that a uniaxial stress applied along the *c* axis would have a negative impact on the 3D ferromagnetism. This character together with the orbital ordering and the lattice distortion demonstrated in the local angular site distortion in part (1) of the structural study has been used in this work to test rigorously whether 3D ferromagnetism is indeed due to the superexchange interaction. In contrast, the DE model requires delocalized electrons in 3D, which would not produce a particular lattice distortion as far as we know.

## 2. Paramagnetic susceptibility of $\text{La}_{1-x}\text{Sr}_x\text{MnO}_3$

As shown in the phase diagram of  $\text{La}_{1-x}\text{Sr}_x\text{MnO}_3$  of Fig.3 and the transport properties of the  $x=0.125$  sample demonstrated in the next section, the paramagnetic phase in the underdoped range is an insulator. Moreover, samples in this doping range undergo two structural transitions  $\text{O}'/\text{O}^*$  at  $T_{\text{oo}}$  ( $\text{O}'$  is the orthorhombic phase with a cooperative orbital order distortion and  $\text{O}^*$  is the orbitally disordered phase) and  $\text{O}^*$  to the rhombohedral phase at  $T_{\text{OR}}$  as temperature increases. The paramagnetic susceptibility reveals important information about changes of spin-spin exchange interactions due to the structural evolution as well as on crossing the phase transitions. We have measured the magnetic susceptibility from the parent  $\text{LaMnO}_3$  to ferromagnetic  $\text{La}_{0.82}\text{Sr}_{0.18}\text{MnO}_3$  with a fine step of  $x$  in order to reveal in detail how the transformation from 2D ferromagnetism to 3D ferromagnetism evolves. The inverse magnetic susceptibilities for compositions typical for the underdoped range are shown in Fig.4. First of all,  $\chi^{-1}(T)$  of all samples in Fig.4 show a usual Curie-Weiss behavior in a magnetic field  $H=2000$  Oe except for interruptions at the phase transition temperatures  $T_{\text{oo}}$  and  $T_{\text{OR}}$ . The argument for a Griffiths phase<sup>40,41</sup> in the interpretation of an unusual curvature of  $\chi^{-1}(T)$  at  $T > T_c$  found in underdoped  $\text{La}_{1-x}\text{Sr}_x\text{MnO}_3$  was made based on measurements with very low magnetic fields. In those measurements,  $\chi(T)$  is more sensitive to the sample's inhomogeneity and becomes more sample-dependent. We have found a similar anomaly in  $\chi^{-1}(T)$  with  $H=20$  Oe for samples showing much broader transitions at  $T_{\text{oo}}$  and  $T_{\text{OR}}$ . The sharpness of the transition of  $\chi(T)$  at  $T_{\text{oo}}$  and  $T_{\text{OR}}$  is field-independent in our samples, which confirms a good homogeneity.

A Weiss constant  $\theta > 0$  is obtained by fitting the  $\chi^{-1}(T)$  of the parent perovskite  $\text{LaMnO}_3$  with a Curie-Weiss law. However, a  $\theta > 0$  does not mean an overall 3D ferromagnetic coupling. The cooperative JT distortion gives a ferromagnetic coupling through the superexchange  $e^0\text{-O}_2\text{-}e^1$  interaction in the  $ab$  planes whereas an antiferromagnetic interaction via the superexchange  $t^3\text{-O}_1\text{-}t^3$  is present along all crystallographic axes. An NMR measurement, which is a site-selective probe, has indeed confirmed a negative  $\theta$  for the coupling via  $\text{Mn}^{3+}\text{-O}_1\text{-Mn}^{3+}$  and a positive  $\theta$  for the interaction via  $\text{Mn}^{3+}\text{-O}_2\text{-Mn}^{3+}$ .<sup>42</sup> The  $\sigma$ -bonding  $e$  electrons give stronger interactions than those between  $\pi$ -bonding  $t_2$  orbitals. A positive Weiss constant  $\theta$  derived from the bulk susceptibility in Fig.4 is an averaged value. A sharp drop at  $T_N$  in  $\chi^{-1}(T)$  is typical for an antiferromagnet with canted spins.<sup>43</sup> The spin canting structure has been studied with far-infrared

spectroscopy.<sup>44</sup> For the  $x=0.07$  sample, the cooperative orbital order distortion still survives to  $T > 400$  K. The observation of a cooperative orbital order distortion in the mixed valent system  $\text{La}_{1-x}\text{Sr}_x\text{MnO}_3$  means that doped carriers are trapped at immobile  $\text{Mn}^{4+}$  ions to allow the  $\text{Mn}^{3+}$  matrix to order its  $e_g$  electrons cooperatively. While the dilution by a non-JT  $\text{Mn}^{4+}$  reduces  $T_{\text{oo}}$  from 750 K in  $\text{LaMnO}_3$ ,<sup>45,46</sup> the cooperative orbital order distortion on  $\text{Mn}^{3+}$  in the hole doped  $\text{La}_{1-x}\text{Sr}_x\text{MnO}_3$  is similar to that in  $\text{LaMnO}_3$ . The obvious change of  $\chi^{-1}(T)$  for the  $x=0.07$  sample is that the Weiss  $\theta$  derived from fitting  $\chi^{-1}(T)$  to a CW law, while it is still smaller than  $T_N$ , is close to  $T_N$ . An enhanced 3D ferromagnetic component in this case is caused by both the superexchange  $e^0\text{-O}_2\text{-e}^1$  and  $e^0\text{-O}_1\text{-e}^1$  surrounding the trapped holes and the orbital mixing in the matrix of  $\text{Mn}^{3+}$  as in  $\text{LaMn}_{1-x}\text{Ga}_x\text{O}_3$ . A  $\theta > T_c$  found for the samples with  $x \geq 0.1$  makes them fulfill the classic criteria for 3D ferromagnetism. The cooperative orbital order transition leads to an abrupt anomaly in  $\chi^{-1}(T)$  at  $T_{\text{oo}}$ , which decreases progressively as  $x$  increases in  $\text{La}_{1-x}\text{Sr}_x\text{MnO}_3$ . The structural transition from the orthorhombic phase to the rhombohedral phase at  $T_{\text{OR}}$  causes a similar anomaly in  $\chi^{-1}(T)$  for samples with  $x \geq 0.145$  in the temperature range  $T < 400$  K. For a given composition, a higher Weiss  $\theta$  is always found in the phase above  $T_{\text{oo}}$  and  $T_{\text{OR}}$ . These observations highlight further that the magnetism in underdoped  $\text{La}_{1-x}\text{Sr}_x\text{MnO}_3$  is closely coupled to the crystal structure. The fitting results of the  $\chi(T)$  data are summarized in Fig.5. A vertical line near  $x=0.09$  separates the antiferromagnetism with  $T_N > \theta$  and 3D ferromagnetism with  $T_c < \theta$ . The Weiss constant  $\theta$  increases with  $x$  in both the AF phase and the F phase. However, there is a clear slope change on crossing the vertical line. The first point of  $\theta$  in the O\* and R phases in the plot may have larger uncertainty since these data were from the fitting over a relatively narrow temperature range. It is interesting to note that  $\theta(x)$  can be fit linearly in all three O', O\* and R phases with an identical slope.

Although  $\theta(x)$  tracks more or less the change in  $T_c$  as a function of  $x$ , a ferromagnetic spin ordering in manganites opens a new channel for electron hopping at  $T < T_c$ , which in turn alters the magnetic coupling. We have previously identified a polaronic to itinerant electronic transition at  $T < T_c$  in underdoped manganites under pressure.<sup>47,48</sup> A clear enhancement of  $T_c$  has been found on crossing the electronic transition. These changes are certainly not reflected in the  $\theta(x)$  in Fig.5 since  $\theta$  is extracted in the paramagnetic insulator phase.

To this point, we have demonstrated that the superexchange interaction can account for the change of magnetic coupling in the phase with cooperative orbital ordering. One may be curious why a maximum  $T_c$  is only about 60 K in  $\text{LaMn}_{1-x}\text{Ga}_x\text{O}_3$  whereas it is about 200 K in  $\text{La}_{1-x}\text{Sr}_x\text{MnO}_3$  given a similar local site distortion in Fig. 2 and therefore a similar orbital mixing achieved by either Ga or Sr doping. First of all, it is impossible to have a cooperative orbital ordering of all  $\text{Mn}^{3+}$  that delivers a 3D  $e^0\text{-O-}e^1$  ferromagnetic interaction. In the case of Ga substitution, the superexchange interaction occurs only through the connections within the  $\text{Mn}^{3+}\text{-O-Mn}^{3+}$  array and the ferromagnetic coupling along the  $c$  axis sets in as the orbital mixing is large enough. In comparison, on top of the orbital mixing in the  $\text{Mn}^{3+}\text{-O-Mn}^{3+}$  array, the minority  $\text{Mn}^{4+}$  with empty  $e_g$  orbitals creates more chances of making a ferromagnetic  $e^0\text{-O-}e^1$  bonding with neighboring  $\text{Mn}^{3+}$ . The same story may also be applicable to the orbitally disordered phase. A jump of  $\theta$  on crossing  $T_{oo}$  can be attributed to two factors (a) an increase of Mn-O-Mn bond angle<sup>16</sup> that increases the overlap integral in the superexchange interaction and (b) disordered  $e_g$  orbitals yield more chances to form a ferromagnetic  $e^0\text{-O-}e^1$  bonding through  $\text{Mn}^{3+}\text{-O-Mn}^{3+}$  and  $\text{Mn}^{4+}\text{-O-Mn}^{3+}$  interactions. For the  $x=0.14$  sample,  $T_{oo}$  vanishes and a transition to the rhombohedral phase occurs at  $T_{OR} \approx 370$  K. Like  $T_{oo}$ ,  $T_{OR}$  is suppressed progressively as  $x$  increases and it vanishes for  $x \geq 0.18$ . In the rhombohedral phase, the space group does not allow the orbital order distortion. Any orbital order distortion in this case must be dynamic. A jump of  $\theta$  on crossing  $T_{OR}$  can be attributed to an increase of the Mn-O-Mn bond angle<sup>16</sup> in the superexchange interaction. However, a much improved electronic conductivity in the heavily doped rhombohedral phase may let the DE interaction kick in progressively with  $x$  in the paramagnetic phase.

### 3. The correlation between transport properties and magnetic coupling in $\text{La}_{0.875}\text{Sr}_{0.125}\text{MnO}_3$

We have chosen to study the temperature dependences of resistivity  $\rho$ , thermoelectric power  $S$ , thermal conductivity  $\kappa$ , and magnetization of the  $x=1/8$  sample since it undergoes several important phase transitions as temperature decreases. As shown in Fig.6, the cooperative orbital ordering at  $T_{oo} \sim 275$  K causes a sharp anomaly in the curve of  $\chi^{-1}$  versus  $T$ ; it only reduces the Weiss constant in the paramagnetic susceptibility on cooling down through  $T_{oo}$ . Nevertheless, a Curie-Weiss fitting to the paramagnetic susceptibility below  $T_{oo}$  gives rise to a Weiss constant  $\theta \geq T_c$  in the ferromagnetic phase. However, as pointed out by de Gennes,<sup>4</sup> Zener carriers with a

bandwidth in the level of  $kT$  do not contribute to the DE interaction in the paramagnetic phase since the hopping time is longer than the time constant of a paramagnetic spin relaxation. We can show a small-polaron conduction in the paramagnetic phase from the following observations. (a) A large activation energy in the conductivity and a large thermoelectric power  $S$ . Moreover, the temperature dependence of  $S$  above  $T_c$  indicates the mobile charge carriers are progressively trapped out as immobile  $Mn^{4+}$  in the matrix of  $Mn^{3+}$  ions. (b) Although the cooperative orbital order restores the thermal conductivity  $\kappa$  very little on cooling through  $T_{co}$ , it is essentially a glassy state for heat transfer in the entire temperature range  $T > T_{co}$ , including both the ferromagnetic spin ordered phase and the paramagnetic phase. A small and glassy  $\kappa$  is normally seen in a phase with small polaron conduction. (c) The  $e_g$  electronic state must be localized for a cooperative orbital ordering to occur at  $Mn^{3+}$  sites in this mixed valent system. These observations support the argument that the magnetic coupling in the paramagnetic phase is primarily from the superexchange interaction and the coupling leads to a normal ferromagnetic transition at  $T_c$ . Drops of thermoelectric power and resistivity at  $T \leq T_c$  indicate that trapped small polarons start to become mobile in the ferromagnetic phase. The temperature range for the conducting ferromagnetic phase is narrow; the conducting phase in  $T < T_c$  allows trapped  $Mn^{4+}$  to move, which makes possible a transition from randomly trapped  $Mn^{4+}$  in the phase at  $T > T_c$  to a charge ordered insulator phase at  $T < T_{co}$ . The number of hopping polarons is sharply reduced at  $T \leq T_{co}$  as indicated by a jump of  $S$ . Although there is no agreement on the detailed pattern of how charges or polarons and orbitals become ordered at  $T < T_{co}$ ,<sup>49-60</sup> they must be well ordered at  $T < T_{co}$  as seen from a sharp increase of the thermal conductivity. Ferromagnetism should collapse at  $T \leq T_{co}$  if the magnetic coupling is due to a real charge transfer. Instead, the magnetization shows a small jump on cooling through  $T_{co}$ , see Fig.7. This observation means that the magnetic coupling has little to do with the charge transport, but depends critically on the structural change. The lattice distortion at  $T \leq T_{co}$  is actually consistent with the picture of orbital mixing, *i.e.* the percentage of the  $e_g$  electron occupation along the  $c$  axis is considerably increased. As a result, the  $c$  axis expands at  $T \leq T_{co}$ . The peculiar change of lattice parameters due to the orbital mixing will be further verified with the magnetization measurements under uniaxial stress. In summary: (a) small-polaron conduction does not provide a ferromagnetic coupling in the paramagnetic phase of the underdoped  $La_{1-x}Sr_xMnO_3$ , (b) the

orbital mixing in the charge/orbital ordered phase at  $T < T_{co}$  in the  $x=1/8$  phase optimizes the ferromagnetic coupling through a superexchange interaction.

#### 4. Uniaxial stress effects on the cooperative orbital order, orbital mixing, and magnetism in $\text{La}_{0.875}\text{Sr}_{0.125}\text{MnO}_3$ and $\text{LaMn}_{0.5}\text{Ga}_{0.5}\text{O}_3$

As shown in Fig.6, the  $M(T)$  of the  $x=0.125$  crystal changes abruptly at  $T_{co}$ ,  $T_c$ , and  $T_{oo}$ . We have monitored changes of these transition temperatures as uniaxial stress is applied along different crystallographic axes of a  $\text{La}_{0.875}\text{Sr}_{0.125}\text{MnO}_3$  crystal. Experimental data are shown in Fig.7 and a summary of the transition temperatures versus uniaxial stress is displayed in Fig.8. Since the phase in the interval  $T_{co} < T < T_{oo}$  is characterized by a shorter  $c$  axis, see Fig.9, a uniaxial stress along the  $c$  axis,  $P_c$ , should stabilize this phase and we indeed have found a  $dT_{oo}/dP_c > 0$ . A giant coefficient  $dT_{oo}/dP_c = 12 \text{ K/kbar}$  obtained by linear fitting the data of  $T_{oo}$  versus  $P_c$  indicates that the orbital ordering below  $T_{oo}$  is strongly coupled to the lattice. Although the ferromagnetic spin ordering at  $T_c$  does not alter the orbital ordering, a slight increase of the  $c$  axis below  $T_c$  from the structural study<sup>5</sup> predicts a  $dT_c/dP_c \leq 0$ . The  $T_c$  versus  $P_c$  in Fig.8 is consistent with this prediction. The observed  $dT_c/dP_c \leq 0$  also indicates the ferromagnetism below  $T_c$  depends sensitively on the  $e_g$  orbital occupation along the  $c$  axis.

The transition on cooling through  $T_{co}$  is accompanied by an increase of the  $c$  axis.<sup>55</sup> We have obtained a  $dT_{co}/dP_c = -15 \text{ K/kbar}$ , which is similar to  $dT_{oo}/dP_c$  in magnitude, but has opposite sign. These observations indicate that the uniaxial-stress dependences of  $T_{oo}$  and  $T_{co}$  are basically determined by the discontinuous jump/drop of the  $c$  axis as described by the Clausius-Clapeyron (CC) relation  $dT_{co(oo)}/dP_c = V_m \Delta(\Delta c/c) / \Delta S$ , where  $V_m$  is the mole volume,  $\Delta S$  is the total entropy change on crossing the transition. By taking a  $\Delta S \approx 600 \text{ mJ/mole K}$  from the specific-heat measurement<sup>61</sup> and  $\Delta(\Delta c/c) \approx 4.5 \times 10^{-3}$  from the temperature dependences of lattice parameters,<sup>55</sup> we have obtained a  $dT_{co}/dP_c = 26 \text{ K/kbar}$ . The consistency between the measured coefficient and the calculated value through the CC relation is remarkable given that the uncertainty of the thermal expansion jump at  $T_{co}$  calculated from the XRD data is large and the whole crystal may not experience the uniaxial stress uniformly.

In the parent compound  $\text{LaMnO}_3$ ,  $e_g$  electrons are ordered into primarily  $3x^2-r^2/3y^2-r^2$  orbitals in  $ab$  planes and the orbital mixing effect is negligible, which leads to a reduction of  $c/\sqrt{2}$ . Like the Ga substitution in  $\text{LaMn}_{1-x}\text{Ga}_x\text{O}_3$ ,<sup>39</sup> the Sr doping in  $\text{La}_{1-x}\text{Sr}_x\text{MnO}_3$  enhances the orbital mixing, which causes an evolution from 2D ferromagnetism (type-A antiferromagnetism) in  $\text{LaMnO}_3$  to 3D ferromagnetism for compositions  $x \geq 0.1$  in  $\text{La}_{1-x}\text{Sr}_x\text{MnO}_3$ . The orbital order transition in the Sr doped  $\text{La}_{1-x}\text{Sr}_x\text{MnO}_3$ , while causing a similar lattice distortion as in the parent perovskite, occurs at a significantly lower temperature;  $T_{\text{oo}} = 275$  K for the  $\text{La}_{0.875}\text{Sr}_{0.125}\text{MnO}_3$  crystal (it is 750 K in  $\text{LaMnO}_3$ ). We expect a similar uniaxial stress effect on  $T_{\text{oo}}$  in  $\text{LaMnO}_3$  and  $\text{La}_{0.875}\text{Sr}_{0.125}\text{MnO}_3$  based on the change of lattice parameters at  $T_{\text{oo}}$ . However, the cooperative orbitally ordered phase of  $\text{La}_{0.875}\text{Sr}_{0.125}\text{MnO}_3$  supports ferromagnetism as seen from the paramagnetic susceptibility of Fig.4 and Fig.6, which means a higher degree of orbital mixing and therefore a relatively larger  $c$  axis than that in  $\text{LaMnO}_3$ . A uniaxial stress along the  $c$  axis, while enhancing  $T_{\text{oo}}$ , suppresses the ferromagnetic transition by reducing the  $c$  axis and therefore the orbital mixing. In sharp contrast, a uniaxial stress along the  $c$  axis enhances  $T_N$  in  $\text{LaMnO}_3$  since the magnetic coupling for type-A spin ordering is optimized where the cooperative orbital ordering has less orbital mixing. The change from  $dT_N/dP_c > 0$  in  $\text{LaMnO}_3$  to  $dT_c/dP_c < 0$  in  $\text{La}_{0.875}\text{Sr}_{0.125}\text{MnO}_3$  reflects unambiguously that orbital mixing plays an important role in the evolution of magnetism. Since  $\text{Mn}^{4+}$  are trapped in the interval  $T_c < T < T_{\text{oo}}$ , as seen by the  $S(T)$  data in Fig.6, charge ordering depends on mobilizing the  $\text{Mn}^{4+}$  ions below  $T_c$ . Therefore, a reduction of  $T_c$  also reduces  $T_{\text{CO}}$ , and  $T_{\text{CO}}$  of the  $x=0.125$  phase drops dramatically under a uniaxial stress along the  $c$  axis,  $P_c$ . The strength of the ferromagnetic coupling is seen to depend critically on a small structural change, *viz.* the  $\text{Mn-O}_1$  bond length that monitors the degree of orbital mixing. In summary:  $T_{\text{oo}}$  is progressively suppressed with increasing  $x$  in hole-doped  $\text{La}_{1-x}\text{Sr}_x\text{MnO}_3$  owing to the dilution by JT-inactive  $\text{Mn}^{4+}$  in the matrix of JT-active  $\text{Mn}^{3+}$  ions. A  $P_c$  stabilizes the occupied  $e_g$  orbitals more into the basal plane, which reduces the orbital mixing responsible for 3D ferromagnetic coupling, therefore reducing  $T_c$  and therefore  $T_{\text{CO}}$  also; but it increases  $T_{\text{oo}}$  by creating a better match between the JT distortion and the bias of the intrinsic octahedral-site distortion.

A cooperative JT orbital ordering of  $3y^2-r^2/3x^2-r^2$  at a  $T < T_{\text{JT}}$  would give a tetragonal structural distortion. It remains true even if the orbital mixing is taken into account. The orthorhombic



structure found in underdoped  $\text{La}_{1-x}\text{Sr}_x\text{MnO}_3$  is due to the bias effect from the intrinsic site distortion of the  $Pbnm$  perovskite.<sup>11,12</sup> The orthorhombic structure, especially the interaction between orbital ordering and the local site distortion discussed in the structural section, discriminates the effects of uniaxial stress as it is applied along the  $a$  and  $b$  axes, which is discussed in the next section.

Based on the lattice-parameter changes at  $T_{oo}$  and  $T_{co}$ <sup>55</sup> in Fig.9 and the CC relation, we expect to see  $dT_{oo}/dP_{a,b} < 0$  and  $dT_{co}/dP_{a,b} > 0$ . Fig.8 indeed shows that  $T_{JT}$  decreases and both  $T_c$  and  $T_{co}$  increase slightly at lower values of  $P_a$  and  $P_b$ . Surprisingly, the trend of  $T_{oo}$  versus  $P_a$  or  $P_b$  reverses at a critical stress. At nearly the same stress, the signs of both  $dT_c/dP_{a,b}$  and  $dT_{co}/dP_{a,b}$  reverse too. It is also important to note that the stress dependences of transition temperatures are more gradual for the uniaxial stress along the  $a$  axis than along the  $b$  axis. The maximum uniaxial stress applied before crushing the crystal is below 500 bar. Such a low stress used should have a negligible effect on bond lengths and bond angles and therefore on the overlap integrals; but they are likely to influence the orientation of orbital ordering and the orbital mixing at  $T_{oo}$  if a uniaxial stress is applied in the orbitally disordered phase. In order to understand why the uniaxial stress triggers dramatic changes of  $T_{oo}$ ,  $T_c$ , and  $T_{co}$ , we need to use the major conclusions from the structural study presented in the first two sections. As shown in the phase diagram of Fig.3, the phase boundary  $T_{oo}$  can be crossed by varying either  $x$  at a given temperature or temperature at a given  $x$ . Let's take the  $x = 1/8$  sample and monitor the changes of physical properties by varying temperature. On cooling through  $T_{oo}$ , the cooperative orbital ordering places the  $e_g$  electron primarily into an orbital in the  $ab$  plane; the orbital ordering corresponds to a slight expansion of the  $ab$  plane and reduction of the  $c$  axis, as shown schematically in Fig.10(a,b, d). The cooperative orbitally ordered phase prefers a smaller intrinsic angle distortion, *i.e.* an  $\alpha \approx 90^\circ$ . The interaction between the cooperative orbital order and the angular site distortion contributes an additional jump of the  $b$  axis to give rise to a  $b > a$  from a  $b < a$  in the orbitally ordered phase. Under the circumstance that both  $a$  and  $b$  jump on cooling through  $T_{oo}$ , a sufficiently high loading force applied along the  $a$  or  $b$  axis at room temperature would create an anomalously high stress as it is cooled down through  $T_{oo}$ , which makes the orbital ordering unstable against a new orbital orientation, *i.e.* a turning of ordered orbitals globally by  $90^\circ$  as illustrated in Fig.10 (c, e). The shortest axis in the new orientation of

orbital ordering is now along the uniaxial-stress direction. Therefore, a further reduction of the new shortest axis makes  $T_{oo}$  increase in Fig. 10. On cooling through  $T_{oo}$ , the  $b$  axis expands more dramatically than the  $a$  axis, signaling that the intrinsic  $\alpha < 90^\circ$  is playing a role. This difference accounts for dramatic changes in the curves of  $T_{oo}$ ,  $T_c$ ,  $T_{co}$  versus  $P_b$ , which is in contrast to the relatively gradual changes found for those with  $P_a$ . Now we come to the issue why the trend of  $T_{co}$  versus  $P_{a,b}$  is also reversed at the critical uniaxial stress that triggers a new orbital orientation below  $T_{oo}$ . The correlation between  $dT_{co}/dP_{a,b}$  and  $dT_{oo}/dP_{a,b}$  is not expected in any model in the literature about the charge and orbital ordering below  $T_{co}$ . At a stress above the critical value, the new orientation of the orbital ordering turns the new  $c$  axis along the  $a$  or  $b$  axis. Based on the orbital mixing model, a reduced new  $c$  axis decreases the orbital mixing along this direction, which destabilizes the ferromagnetic state below  $T_c$  and  $T_{co}$ .

Since the evolution from 2D to 3D FM coupling in the single-valent system  $\text{LaMn}_{1-x}\text{Ga}_x\text{O}_3$  has been well-explained with a superexchange model,<sup>39</sup> we have performed the identical experiments on a ferromagnetic  $\text{LaMn}_{0.5}\text{Ga}_{0.5}\text{O}_3$  crystal in order to verify whether ferromagnetism in both  $\text{LaMn}_{1-x}\text{Ga}_x\text{O}_3$  and in the underdoped  $\text{La}_{1-x}\text{Sr}_x\text{MnO}_3$  are indeed due to the same origin. The structural studies show an increase with  $x$  of the  $c$ -axis.<sup>38,39</sup> The enhancement of the orbital mixing leads to 3D ferromagnetism.<sup>39</sup> Therefore,  $T_c$  should be reduced if stress is applied along the  $c$  axis. In contrast, the stress on the  $a$  and  $b$  axis should influence  $T_c$  very little. As shown in Fig. 8 and Fig. 11, these predictions apply very well to  $T_c$  in  $\text{La}_{0.875}\text{Sr}_{0.125}\text{MnO}_3$  and  $\text{LaMn}_{0.5}\text{Ga}_{0.5}\text{O}_3$ . In the  $\text{LaMn}_{0.5}\text{Ga}_{0.5}\text{O}_3$  crystal, the cooperative orbital order occurs above room temperature. As discussed for the  $\text{La}_{0.875}\text{Sr}_{0.125}\text{MnO}_3$  crystal, a modest stress along the  $a$  or  $b$  axis would not trigger the orbital reorientation in this case. The very weak stress dependence of  $T_c$  on  $P_a$  and  $P_b$  is also well-supported by the orbital mixing model. In summary, the uniaxial stresses have the same effect on the ferromagnetic transition temperatures in the single-valent  $\text{LaMn}_{0.5}\text{Ga}_{0.5}\text{O}_3$  and the mixed-valent  $\text{La}_{0.875}\text{Sr}_{0.125}\text{MnO}_3$ .

## Conclusion

Hole doping in the perovskite  $\text{La}_{1-x}\text{Sr}_x\text{MnO}_3$ , a prototype system for studying the CMR effect and the double exchange interaction, changes the intrinsic local structural distortion. Comparison with the simulation calculated with the model assuming rigid octahedra, the experimental results

reveal a strong interaction between the JT orbital ordering and the intrinsic site distortion. The orbitally ordered phase prefers a smaller angular site distortion. The intrinsic bond length splitting distortion biases the cooperative JT orbital ordering and associated orbital mixing. From structural analysis, the doping-induced local structural change causes an orbital mixing that leads to an evolution in the superexchange interactions from 2D ferromagnetic coupling in the parent perovskite  $\text{LaMnO}_3$  to a 3D ferromagnetic coupling in  $\text{La}_{1-x}\text{Sr}_x\text{MnO}_3$  with  $x > 0.08$ . The paramagnetic phase of underdoped  $\text{La}_{1-x}\text{Sr}_x\text{MnO}_3$  is an insulator. The Weiss constant extracted from the paramagnetic susceptibility of the ferromagnetic phase predicts the correct Curie temperature. Therefore, the superexchange interaction, not the DE interaction, is responsible for the ferromagnetic spin ordering in this mixed valent system. The orbital ordering and orbital mixing is associated with particular intrinsic lattice distortions. This correlation allows us to test our model by measuring the magnetization under uniaxial stress. We have demonstrated the manipulation of orbital ordering and orbital mixing with uniaxial stress applied along major crystallographic axes. The results indeed confirm our superexchange interaction model. Surprisingly, we have observed the reorientation of orbital ordering under a modest stress, which indicates orbital orientation degeneracy in the orthorhombic perovskite structure. This finding is important for exploring the orbital dynamics in future studies. In addition, we have made a side-by-side comparison of the uniaxial stress effect on transition temperatures in  $\text{La}_{0.875}\text{Sr}_{0.125}\text{MnO}_3$  and  $\text{LaMn}_{0.5}\text{Ga}_{0.5}\text{O}_3$ . Given that the model of a superexchange interaction is well accepted in  $\text{LaMn}_{0.5}\text{Ga}_{0.5}\text{O}_3$ , the identical uniaxial stress effects found in both systems have further confirmed that the superexchange interaction plays the dominant role in the ferromagnetism found in underdoped  $\text{La}_{1-x}\text{Sr}_x\text{MnO}_3$ .

### **Acknowledgements**

This work was supported by NSF (DMR 1122603). JSZ thanks J.G. Cheng for helping to orient crystals.

\*jszhou@mail.utexas.edu

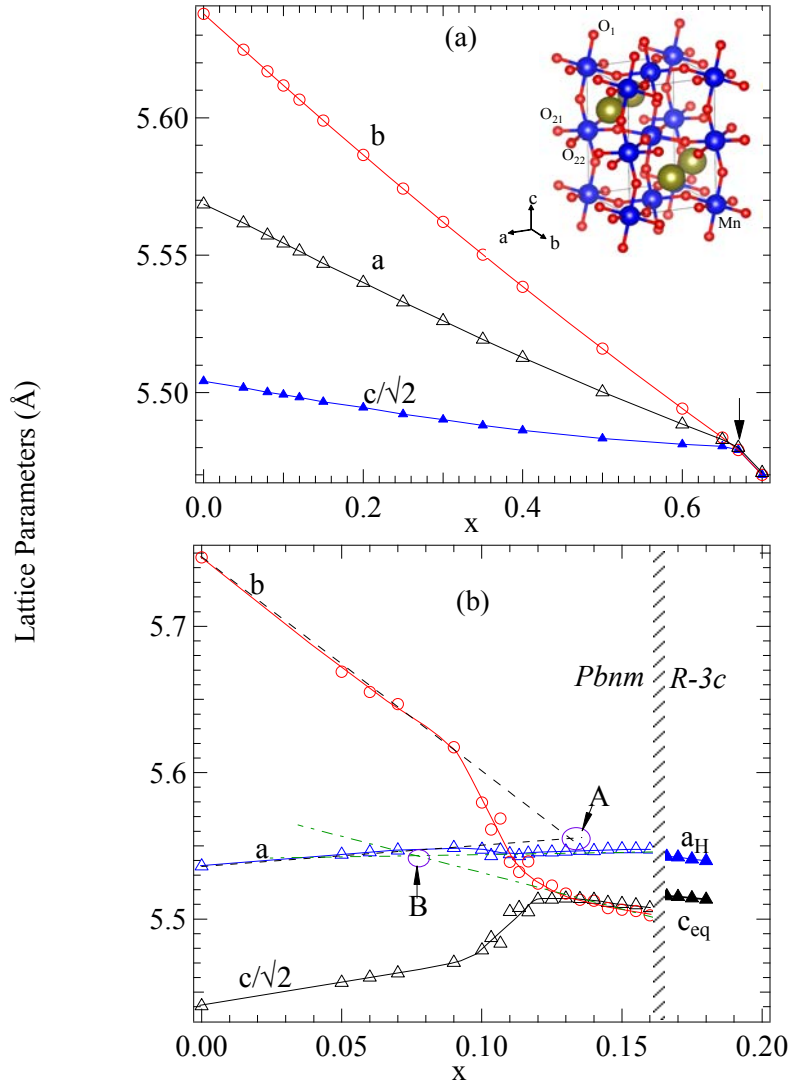


Fig.1 (Color online) Lattice parameters versus Sr doping for  $\text{La}_{1-x}\text{Sr}_x\text{MnO}_3$  (a) the simulation by using the software SPuDS; the arrow points to the critical density of hole doping where a cubic phase is obtained by continuously reducing the octahedral-site tilting in the orthorhombic phase; inset: the structural model of orthorhombic  $Pbnm$   $\text{LaMnO}_3$ . (b) Results from refinements of XRD patterns;  $c_{eq} = (c_h^2 + 12a_h^2)/18$  in the  $R-3c$  phase. Error bars are smaller than the size of symbols.

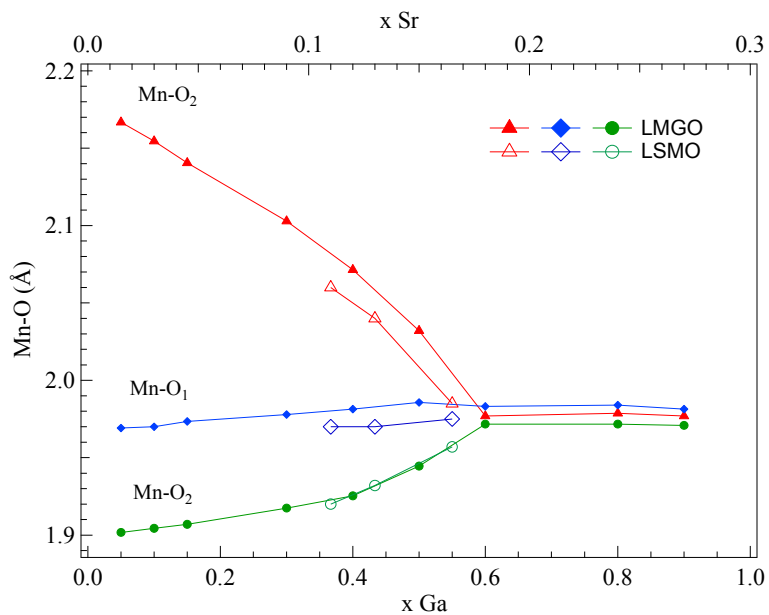


Fig.2 The local bond length splitting as a function of substitution  $x$  in  $\text{La}_{1-x}\text{Sr}_x\text{MnO}_3$  and  $\text{LaMn}_{1-x}\text{Ga}_x\text{MnO}_3$ .

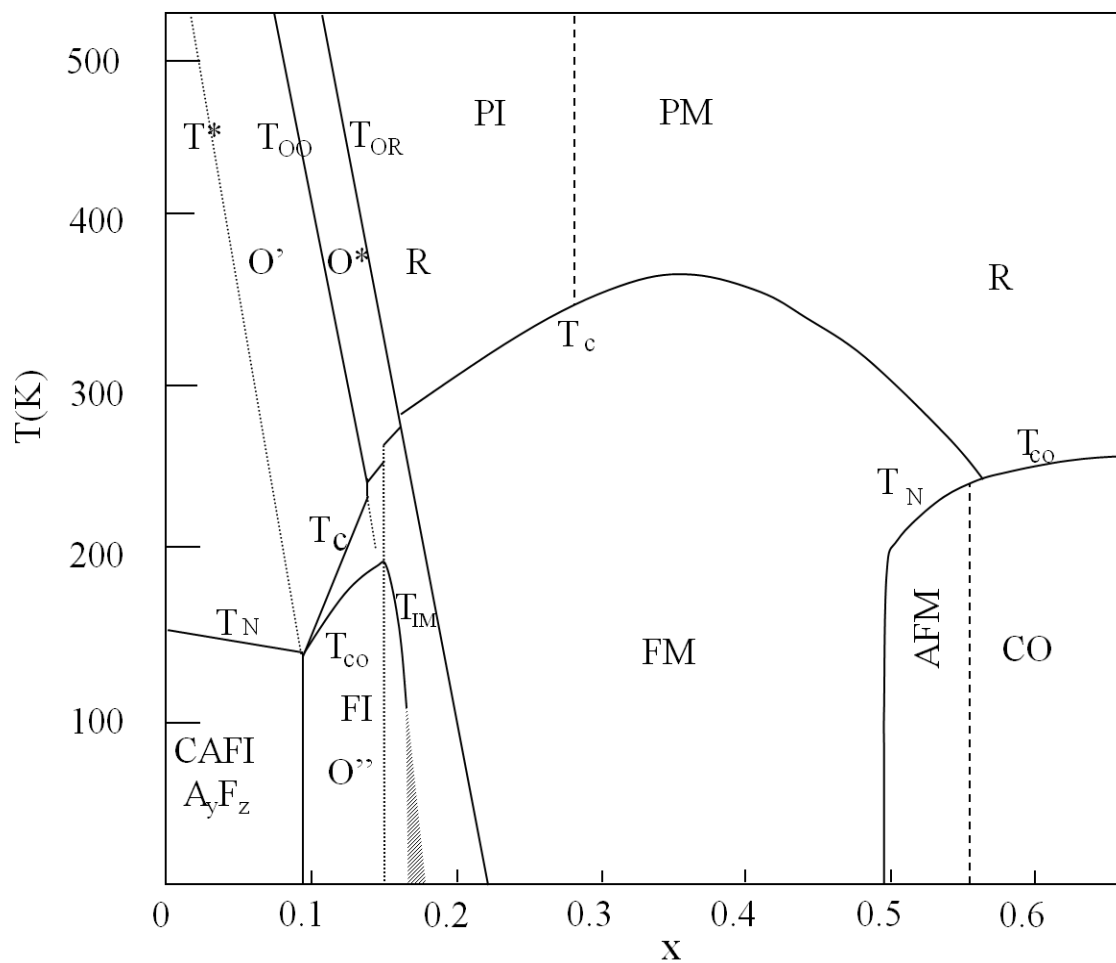


Fig.3 The schematic phase diagram of  $\text{La}_{1-x}\text{Sr}_x\text{MnO}_3$ .

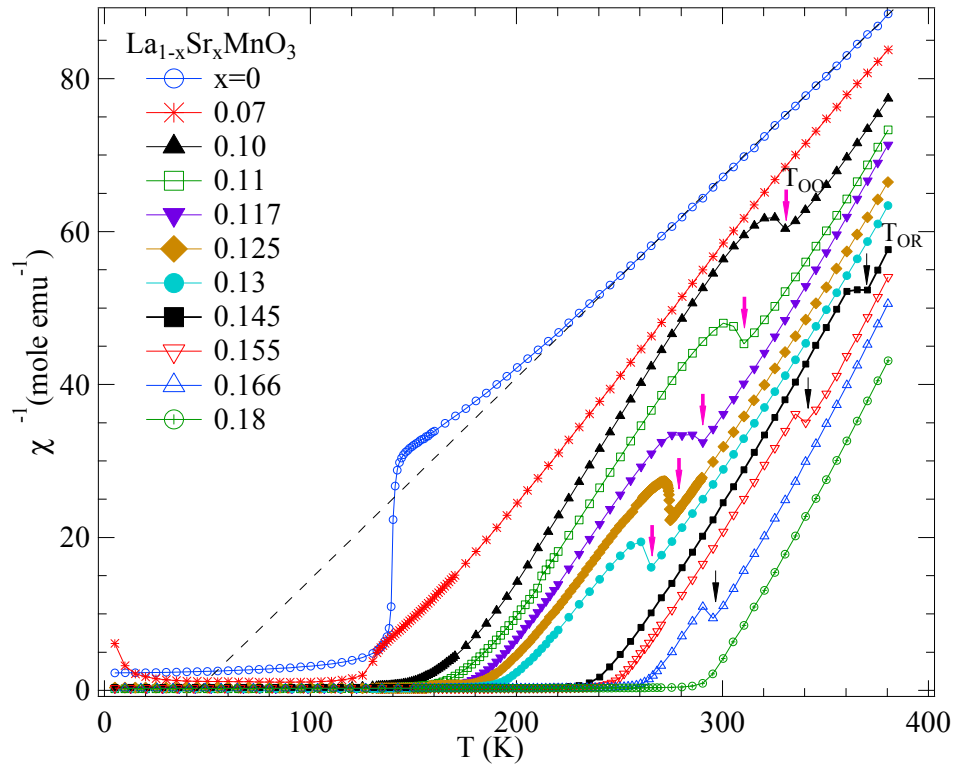


Fig.4 Temperature dependence of inverse magnetic susceptibility for  $\text{La}_{1-x}\text{Sr}_x\text{MnO}_3$ .

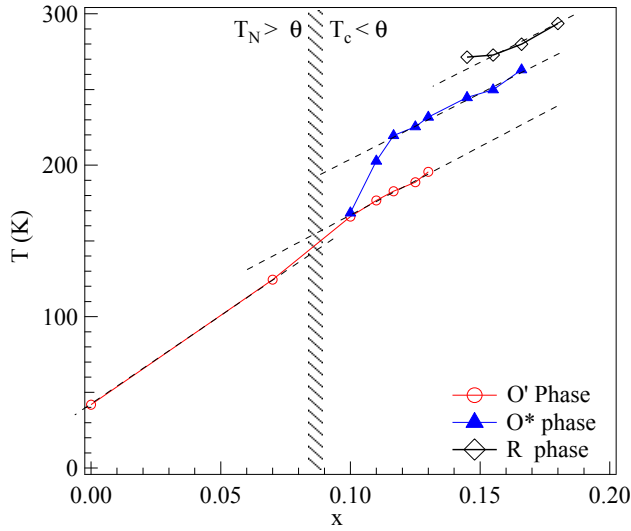


Fig.5 The Weiss constant from a Curie-Weiss fitting of the paramagnetic susceptibility for  $\text{La}_{1-x}\text{Sr}_x\text{MnO}_3$ .

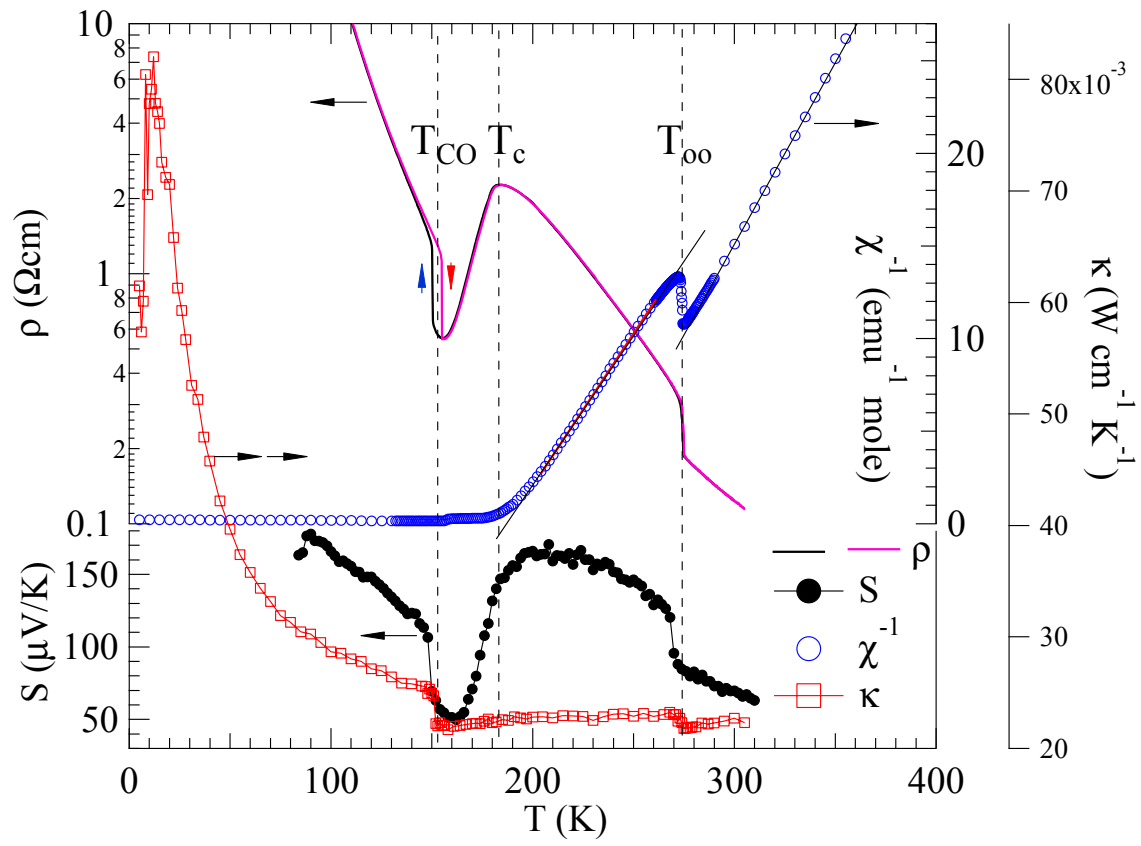


Fig.6 Temperature dependences of resistivity  $\rho$ , inverse magnetic susceptibility  $\chi^{-1}$ , thermoelectric power  $S$ , and thermal conductivity  $\kappa$  of  $\text{La}_{0.875}\text{Sr}_{0.125}\text{MnO}_3$  crystal.



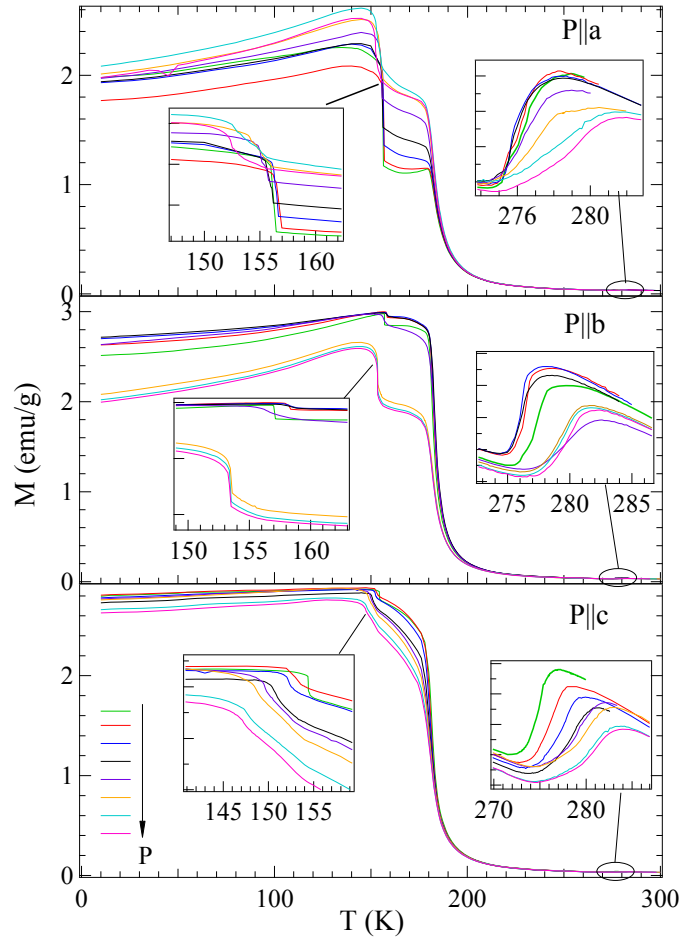


Fig. 7 Temperature dependences of the magnetization of  $\text{La}_{0.875}\text{Sr}_{0.125}\text{MnO}_3$  crystal under uniaxial stress.

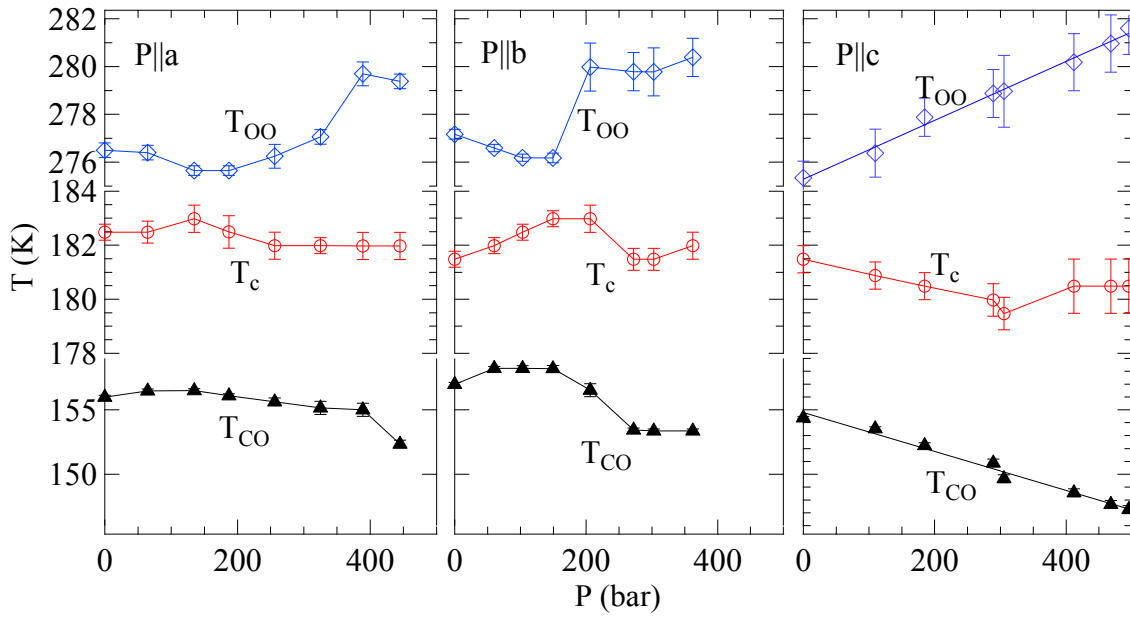


Fig.8 Stress dependences of  $T_{JT}$ ,  $T_c$ , and  $T_{CO}$  of a  $\text{La}_{0.875}\text{Sr}_{0.125}\text{MnO}_3$  crystal. Lines in the right panel are linear fittings to the data of  $T_{JT}$  and  $T_{CO}$  versus stress  $P_c$ .

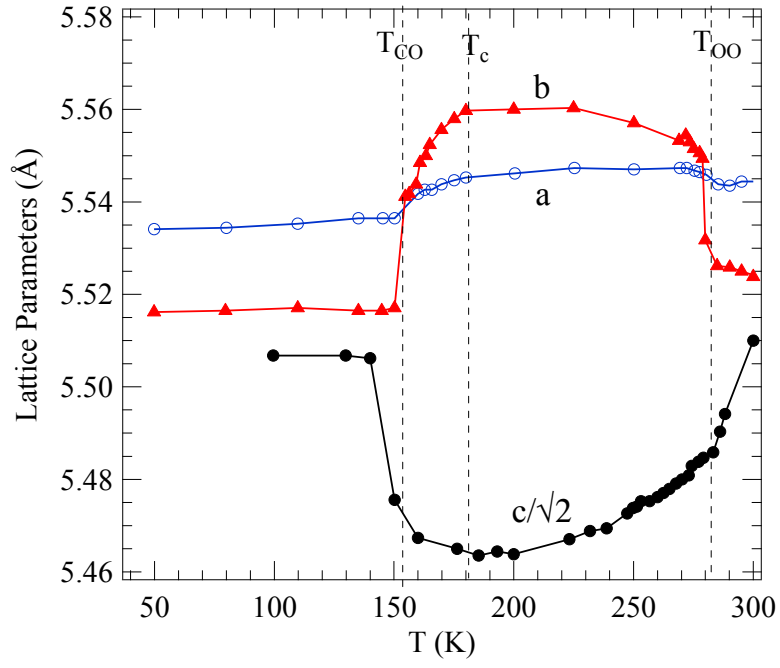


Fig.9 Temperature dependence of lattice parameters of  $\text{La}_{0.875}\text{Sr}_{0.125}\text{MnO}_3$ ; the data are from ref.55

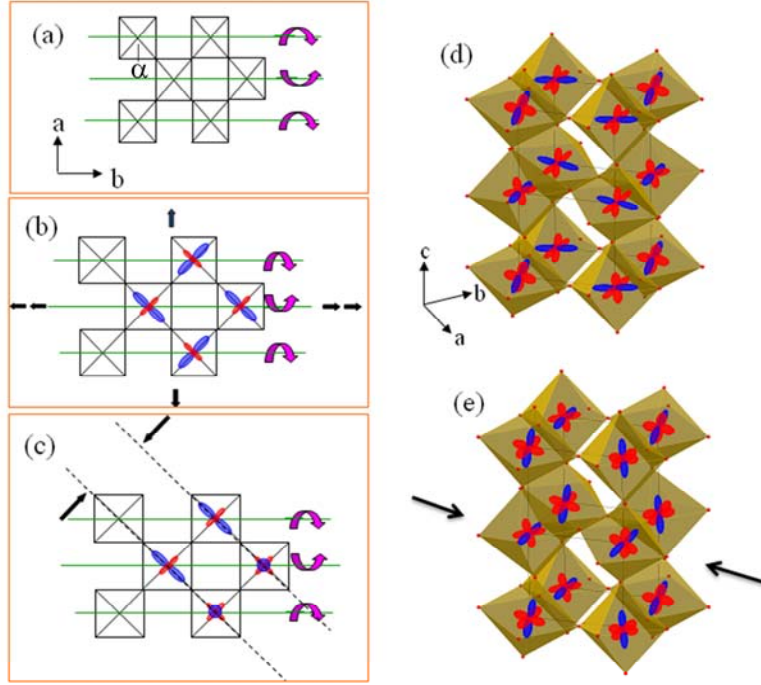


Fig.10 Schematic drawings of the lattice distortions and orbital ordering. (a) The OD phase; (b) The OO phase at  $T < T_{JT}$ ; arrows indicate the lattice expansion. (c) Orbitals rotate under  $P_a$  or  $P_b$  so as to place the shortest axis in the direction of  $P_a$  or  $P_b$ . (d, e) 3D views of the orbital orderings without/with the uniaxial stress applied in the basal plane.

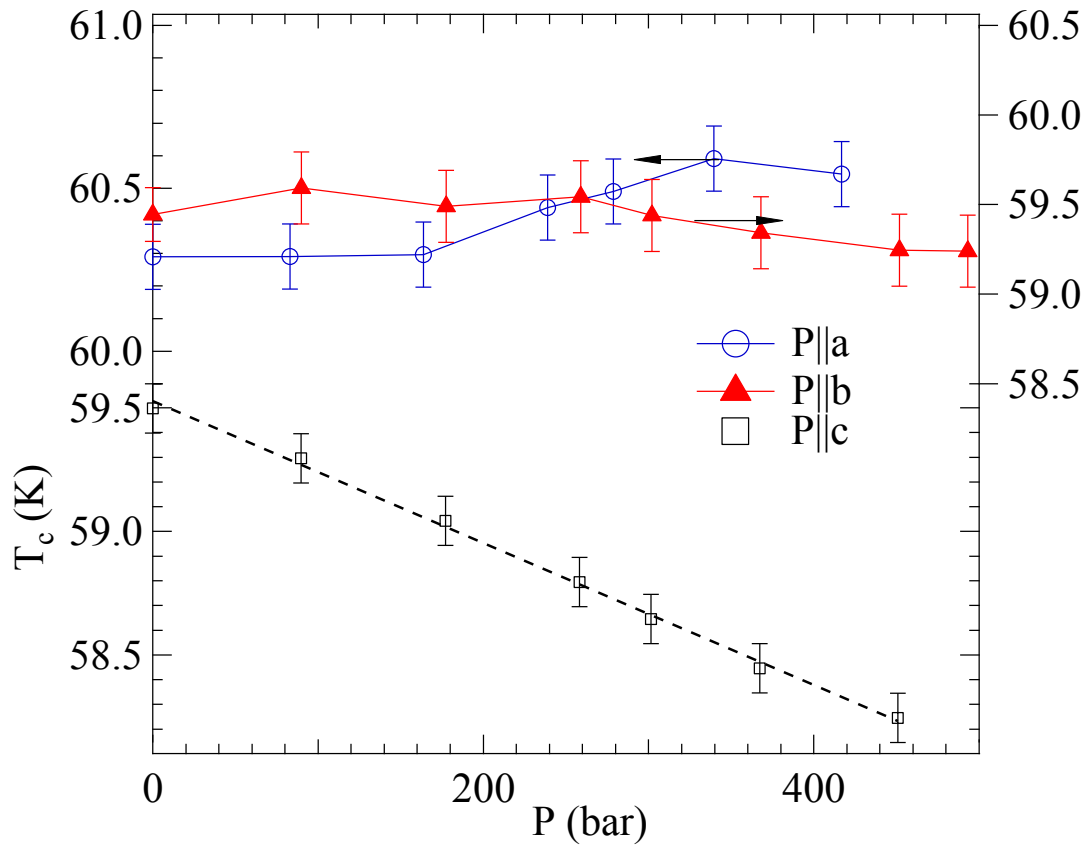


Fig.11 Stress dependence of  $T_c$  in a  $\text{LaMn}_{0.5}\text{Ga}_{0.5}\text{O}_3$  crystal. The dashed line in the plot is a linear fit to the data of  $T_c$  versus  $P_c$ .

## References

1. C. Zener, Phys. Rev. 82, 403 (1951)
2. P.W. Anderson and H. Hasegawa, Phys. Rev. 100, 675 (1955)
3. P.W. Anderson, Magnetism, **1**, 25, ed. by G.T. Rado and H. Suhl (Academic Press, NY1965)
4. P.G. de Gennes, Phys. Rev. 118, 141 (1960)
5. A.J. Millis, Colossal Magnetoresistive Oxides, p53, ed. by Y. Tokura ( Gordon and Breach Science Publishers, Australia 2000)
6. F. Moussa, M. Hennion, J. Rodriguez-Carvajal, H. Moudden, L. Pinsard, and A. Revcolevschi, Phys. Rev. B 54, 15149 (1996)
7. O. Chmaissem, B. Dabrowski, S. Kolesnik, J. Mais, D.E. Brown, R. Kruk, P. Prior, B. Pyles, and J. D. Jorgensen, Phys. Rev. B **64**, 094431 (2001).
8. A. Urushibara, Y. Moritomo, T. Arima, A. Asamitsu, G. Kido, and Y. Tokura, Phys. Rev. B **51**, 14103 (1995).

9. Y. Ishii, M. Kosaka, Y. Uwatoko, A. V. Andreev, and V. Sechovsky, *Physica B* **334**, 160 (2003)
10. J.-S. Zhou and J. B. Goodenough, *Phys. Rev. Lett.* **94**, 065501 (2005).
11. J.-S. Zhou and J. B. Goodenough, *Phys. Rev. B* **77**, 132104 (2008).
12. P. M. Woodward, T. Vogt, D. E. Cox, A. Arulraj, C.N.R. Rao, and A. K. Cheetham, *Chem. Mater.* **10**, 3652 (1998).
13. J.-S. Zhou, J. A. Alonso, V. Pomjakushin, J. B. Goodenough, Y. Ren, J.-Q. Yan, and J.-G. Cheng, *Phys. Rev. B* **81**, 214115 (2010) and references therein.
14. O. Chmaissem, B. Dabrowski, S. Kolesnik, J. Mais, J. D. Jorgensen, and S. Short, *Phys. Rev. B* **67**, 094431 (2003).
15. B. Dabrowski, X. Xiong, Z. Bukowski, R. Dybziński, P. W. Klamut, J. E. Siewenie, O. Chmaissem, J. Shaffer, C. W. Kimball, J. D. Jorgensen, and S. Short, *Phys. Rev. B* **60**, 7006 (1999).
16. X. Xiong, B. Dabrowski, O. Chmaissem, Z. Bukowski, S. Kolesnik, R. Dybziński, C. W. Kimball, and J. D. Jorgensen, *Phys. Rev. B* **60**, 10186 (1999).
17. T. Chatterji, B. Ouladdiaf, P. Mandal, B. Bandyopadhyay, and B. Ghosh, *Phys. Rev. B* **66**, 054403 (2002).
18. G.-L. Liu, J.-S. Zhou, and J. B. Goodenough, *Phys. Rev. B* **64**, 144414 (2001).
19. M. W. Lufaso and P. M. Woodward, *Acta Crystallogr. Sect. B* **57**, 725 (2001).
20. C. J. Howard and H. T. Stokes, *Acta Crystallogr. sect. B* **54**, 782 (1998).
21. J.-S. Zhou, J. A. Alonso, A. Muoz, M. T. Fernandez-Diaz, and J. B. Goodenough, *Phys. Rev. Lett.* **106**, 057201 (2011).
22. T. Hashimoto, N. Matsushita, Y. Murakami, N. Kojima, K. Yoshida, H. Tagawa, M. Dokiya, and T. Kikegawa, *Solid State Comm.* **108**, 691 (1998).
23. M. Baldini, L. Malavasi, D. Di Castro, A. Nucara, W. Crichton, M. Mezouar, J. Blasco, and P. Postorino, arXiv:0807.2848v1 (2008).
24. M. Amboage, M. Hanfland, J. A. Alonso, and M. J. Martinez-Lope, *J. Phys.: Condens. Matter* **17**, s783 (2005).
25. T. Shibusaki, T. Furuya, Y. Takahashi, H. Takahashi, and T. Hashimoto, *J. Thermal Analysis and Calorimetry* **81**, 575 (2005).
26. B. J. Kennedy, T. Vogt, C. D. Martin, J. B. Parise, and J. A. Hriljac, *J. Phys. Condens. Matter* **13**, L925 (2001).
27. R. J. Angel, J. Zhao, N. L. Ross, C. V. Jakeways, S.A. T. Refern, and M. Berkowski, *J. Solid State Chem.* **180**, 3408 (2007).
28. M. Daraktchiev, R. J. Harrison, E. H. Mountstevens, and S.A. T. Redfern, *Mater. Sci. and Engi. A* **442**, 199 (2006).
29. B. J. Kennedy, B. A. Hunter, and J. R. Hester, *Phys. Rev. B* **65**, 224103 (2002).
30. C. J. Howard, K. S. Knight, B. J. Kennedy, and E. H. Kisi, *J. Phys. Condens. Matter* **12**, L677 (2000).

31. E. H. Mountstevens, J. P. Attfield, and S. A.T. Redfern, J. Phys. Condens. Matter **15**, 8315 (2003).
32. B. J. Kennedy, C. J. Howard, and B. C. Chakoumakos, J. Phys. Condens. Matter **11**, 1479 (1999).
33. M. O'Keeffe and B. G. Hyde, Acta Crystallorgr. Sect. B **33**, 3802 (1977).
34. J. B. Goodenough, and J.M. Longo *Crystallographic and Magnetic Properties of Perovskite and Perovskite-Related Compounds*, in *Landolt-Bornstein Tabellan*, edited by K.-H. Hellwege (Springer-Verlag, Berlin, 1970), **New Series III/4a**, Chap. 3, p.126.
35. J. A. Alonso, M. J. Martinez-Lope, M. T. Casais, and M. T. Fernandez-Diaz, Inorg. Chem. **39**, 917 (2000).
36. J. Kanamori, J. Appl. Phys. **31**, S14 (1960)
37. J.-S. Zhou and J.B. Goodenough, Phys. Rev. Lett. **96**, 247202 (2006)
38. J. Blasco, J. Garcia, J. Campo, M.C. Sanchez, and G. Subias, Phys. Rev. B **66**, 174431 (2002)
39. J.-S. Zhou and J.B. Goodenough, Phys. Rev. B **77**, 172409 (2008)
40. J. Deisenhofer, D. Braak, H.A. Krug von Nidda, J. Hemberger, R.M. Eremina, V.A. Ivanshin, A.M. Balbashov, G. Jug, A. Loidl, T.Kimura, and Y. Tokura. Phys. Rev. Lett, **95**, 257202 (2005)
41. M.B. Salamon and S.H. Chun, Phys. Rev. B. **68**, 014411 (2003)
42. A. Trokiner, S. Verkhovskii, A. Gerashenko, Z. Volkova, O. Anikeenok, K. Mikhalev, M. Eremin, and L. Pinsard-Gaudart, Phys. Rev. B **87**, 125142 (2013)
43. V. Skumryev, F. Ott, J.M.D. Coey, A. Anane, J.P. Renard, L. Pinsard-Gaudart, and A. Revcolevschi, Eur. Phys. J.B. **11**, 401 (1999).
44. D. Talbayev, L.Mihaly, and J.-S. Zhou, Phys. Rev. Lett. **93**, 017202 (2004)
45. J. Rodriguez-Carvajal, M. Hennion, F. Moussa, A.H. Moudden, L. Pinsard, and A. Revcolevschi, **57**, R3189 (1998)
46. J.-S. Zhou and J.B. Goodenough, Phys. Rev. B **60**, R15002 (1999)
47. J.-S. Zhou, J.B. Goodenough, A. Asamitsu, and Y. Tokura, Phys. Rev. Lett. **79**, 3243 (1997)
48. J.-S. Zhou and J.B. Goodenough, Phys. Rev. B **62**, 3834 (2000)
49. H. Fujishiro, T. Fukase, and M. Ikebe, J. Phys. Soc. Japan, **67**, 2582 (1998)
50. Y. Yamada, O. Hino, S. Nohdo, R. Kanao, T. Inami, and S. Katano, Phys. Rev. Lett. **77**, 904 (1996)
51. H. Nojiri, K. Kaneko, M, Motokawa, K. Hirota, Y. Endoh, and K. Takahashi, Phys. Rev. B **60**, 4142 (1999)
52. V. Skumryev, J. Nogues, J.S. Munoz, B. Martinez, R. Senis, J.Fontcuberta, L. Pinsard, A. Revcolevschi, and Y.M. Mukovskii, Phys. Rev. B **62**, 3879 (2000)
53. T. Mizokawa, D.I. Khomskii, and G.A. Sawatzky, Phys. Rev. B. **61**, R3776 (2000)
54. J. Nogues, V. Skumryev, J.S. Munoz, B. Martinez, J. Fontcuberta, L. Pinsard, and A. Revcolevschi, Phys. Rev. B **64**, 24434 (2001)

55. J. Geck, P. Wochner, S. Kiele, R. Klingeler, A. Revcolevschi, M.v. Zimmermann, B. Buchner, and P. Reutler, *New J. Phys.* 6, 152 (2004)
56. J. Geck, P. Wochner, D. Bruns, B. Buchner, U. Gebhardt, S. Kiele, P. Reutler, A. Revcolevschi, *Phys. Rev. B* 69, 104413 (2004)
57. J. Geck, P. Wochner, S. Kiele, R. Klingeler, P. Reutler, A. Revcolevschi, B. Buchner, *Phys. Rev. Lett.* 95, 236401 (2005)
58. G. Papavassiliou, M. Pissas, G. Diamantopoulos, M. Belesi, M. Fardis, D. Stamopoulos, A.G. Kontos, M. Hennion, J. Dolinsek, J.-Ph. Ansermet, and C. Dimitropoulos, *Phys. Rev. Lett.* 96, 97201 (2006)
59. Y. Endoh, K. Hirota, S. Ishihara, S. Okamoto, Y. Murakami, A. Nishizawa, T. Fukuda, H. Kimura, H. Nojiri, K. Kaneko, and S. Maekawa, *Phys. Rev. Lett.* 82, 4328 (1999)
60. M. Hennion, F. Moussa, P. Lehouelleur, P. Reutler, and A. Revcolevschi, *Phys. Rev. B.* 73, 104453 (2006)
61. R. Klingeler, J. Geck, R. Gross, L. Pinsard-Gaudart, A. Revcolevschi, S. Uhlenbruck, and B. Buchner, *Phys. Rev. B* 65, 174404 (2002)